Stability of ferrous-iron-rich bridgmanite under reducing midmantle conditions

Sang-Heon Shim[a,1], Brent Grocholski[b,2], Yu Ye[a,c], E. Ercan Alp[d], Shenzhen Xu[e], Dane Morgan[e], Yue Meng[f], and Vitali B. Prakapenka[g]

[a]School of Earth and Space Exploration, Arizona State University, Tempe, AZ 85287; [b]Department of Mineral Sciences, Smithsonian Institution, Washington, DC 20013; [c]State Key Laboratory of Geological Processes and Mineral Resources, China University of Geosciences at Wuhan, 430074 Wuhan, China; [d]Advanced Photon Source, Argonne National Laboratory, Argonne, IL, 60439; [e]Materials Science and Engineering, University of Wisconsin, Madison, WI 53706; [f]Geophysical Laboratory, Carnegie Institute of Washington, Washington, DC 20015; and [g]Center for Advanced Radiation Sources, University of Chicago, Chicago, IL, 60637

Edited by Russell J. Hemley, The George Washington University, Washington, DC, and approved May 9, 2017 (received for review August 22, 2016)

Our current understanding of the electronic state of iron in lower-mantle minerals leads to a considerable disagreement in bulk sound speed with seismic measurements if the lower mantle has the same composition as the upper mantle (pyrolite). In the modeling studies, the content and oxidation state of Fe in the minerals have been assumed to be constant throughout the lower mantle. Here, we report high-pressure experimental results in which Fe becomes dominantly Fe^{2+} in bridgmanite synthesized at 40–70 GPa and 2,000 K, while it is in mixed oxidation state ($Fe^{3+}/\sum Fe = 60\%$) in the samples synthesized below and above the pressure range. Little Fe^{3+} in bridgmanite combined with the strong partitioning of Fe^{2+} into ferropericlase will alter the Fe content for these minerals at 1,100- to 1,700-km depths. Our calculations show that the change in iron content harmonizes the bulk sound speed of pyrolite with the seismic values in this region. Our experiments support no significant changes in bulk composition for most of the mantle, but possible changes in physical properties and processes (such as viscosity and mantle flow patterns) in the midmantle.

bridgmanite | lower mantle | oxidation state | spin transition | bulk sound speed

The variable oxidation state of iron has a profound impact on a range of mantle properties, including the redox conditions and iron partitioning (1, 2). The strong partitioning of trivalent Al into bridgmanite in the lower mantle affects the stability of Fe^{3+} in the phase because the substitution requires defects or charge coupling (3). McCammon (4) reported a large amount of Fe^{3+} ($Fe^{3+}/\sum Fe$ = 60%; fraction of Fe^{3+} with respect to total Fe in a phase) in Al-bearing bridgmanite synthesized in a multianvil press, which was subsequently confirmed under reducing conditions (1, 5). Stabilization of Fe^{3+}–Al charge-coupled substitution and charge disproportionation where $3Fe^{2+}$ (bridgmanite) $\rightarrow 2Fe^{3+}$ (bridgmanite) + Fe^0 (metal) both help explain the large amount of Fe^{3+} under reducing conditions. However, the multianvil studies are limited to ∼800-km depth (26 GPa and 2,300 K). High $Fe^{3+}/\sum Fe$ has been reported in bridgmanite samples synthesized at higher pressures (2, 6–9). However, the existing data are sparse, and bridgmanite has the capacity for large amounts of Fe^{3+} under oxidizing conditions (5, 6, 10). Despite these issues, bridgmanite has been assumed to contain a large amount of Fe^{3+} throughout the lower mantle (1).

The energetics of Fe^{2+} and Fe^{3+} incorporation in bridgmanite, however, can change at higher pressures. Whereas oxygen-defect substitution is energetically competitive for the incorporation of trivalent cations at lower pressures, charge-coupled substitution may be increasingly stabilized at higher pressures (11). Also, the spin configuration of valence electrons in Fe in minerals undergoes changes in the lower mantle (12). Because in bridgmanite the spin behavior of Fe is different depending on the oxidation state and the coordination environment, site preferences of Fe^{3+} and Fe^{2+} change with pressure (13, 14). These factors affect the stable oxidation state and substitution mechanism at different pressures.

We examined the $Fe^{3+}/\sum Fe$ of bridgmanite at a wide range of pressure–temperature conditions related to the lower mantle under reducing conditions. In our experiments, we mixed Fe^{2+}-rich starting materials with approximately bridgmanite stoichiometry with 2–5 wt% Fe metal powder following the method used in multianvil syntheses (1). We enriched all starting materials with 67–95% ^{57}Fe. We loaded the sample mixture into diamond-anvil cells (DACs) together with a pressure medium (*SI Appendix*, Fig. S1). We heated 14 different samples to 2,000–2,300 K at different pressures with the synthesis monitored by using synchrotron X-ray diffraction (XRD) during and after heating (*SI Appendix*, Fig. S2). Energy-dispersive X-ray spectroscopy (EDS) in an aberration-corrected electron microscope (ACEM) showed that the bridgmanite samples synthesized at 47 and 56 GPa contain 0.19 ± 0.02 of Fe# and 0.10 ± 0.03 of Al# on the basis 3 oxygens, which agrees well with the composition of the starting materials within 10% uncertainties from the EDS measurements. Both XRD and ACEM (EDS and imaging) showed that our samples contain bridgmanite and metallic iron (with a small amount of silica only at $P < 40$ GPa), but found no other phases (see *Materials and Methods* and *SI Appendix* for details).

We conducted synchrotron Mössbauer spectroscopy (SMS) on both the temperature-quenched samples at high pressure (hereafter "in situ" SMS) and the decompressed samples at 0–3 GPa and 300 K (hereafter "quench" SMS) (Fig. 1 and *SI Appendix*, Fig. S3). We used quench SMS for $Fe^{3+}/\sum Fe$, because the

Significance

This paper reports an unexpected change in the oxidation state of Fe in bridgmanite, the most dominant mineral in the lower mantle. The oxidation state change resolves the discrepancy between laboratory and seismic studies on the chemical composition of the lower mantle, showing that the lower mantle has major element chemistry similar to the upper mantle. The oxidation state change will also lead to a lower Fe content in bridgmanite in the midmantle, whereas the total Fe content remains the same. Such a change can lead to an increase in viscosity at 1,100- to 1,700-km depths, providing a viable mineralogical explanation on possible viscosity elevation suggested by geophysical studies at the same depth range.

Author contributions: S.-H.S. and B.G. designed research; S.-H.S., B.G., and Y.Y. performed research; E.E.A., Y.M., and V.B.P. contributed new reagents/analytic tools; S.-H.S., B.G., S.X., and D.M. analyzed data; and S.-H.S., B.G., S.X., and D.M. wrote the paper.

The authors declare no conflict of interest.

This article is a PNAS Direct Submission.

[1]To whom correspondence should be addressed. Email: shdshim@gmail.com.

[2]Present address: American Association for the Advancement of Science, Washington, DC 20005.

This article contains supporting information online at www.pnas.org/lookup/suppl/doi:10.1073/pnas.1614036114/-/DCSupplemental.

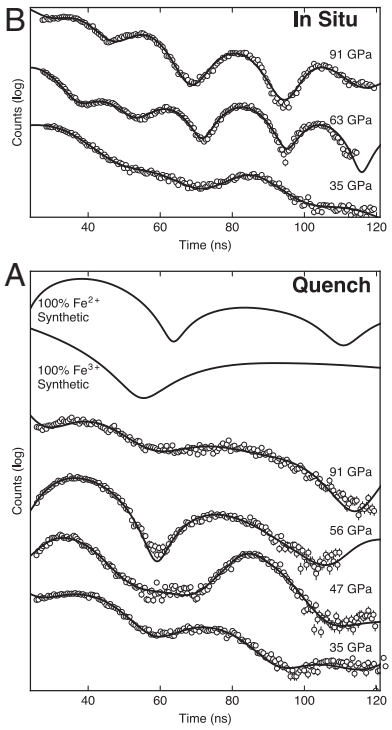

Fig. 1. Synchrotron Mössbauer spectra of bridgmanite. (*A*) Bridgmanite recovered to 0–3 GPa after synthesis at different pressures and 2,000–2,300 K (bottom four spectra). We also included synthetic spectra of bridgmanite at 1 bar with different amount of Fe^{3+} using *IS* and *QS* values from McCammon (4) (top two spectra). (*B*) Bridgmanite at in situ high pressure after laser heating. Synthesis pressures for the samples are shown on the right side (circles, measured intensities; curves, fitted spectra).

quench SMS allows for unambiguous determination of the oxidation state of Fe. The spin effect on isomer shift (IS) and quadrupole splitting (QS) generally overlaps with the oxidation effect at high pressures (*SI Appendix*, section S2 and Fig. S4). The interpretation of the parameters is still controversial at high pressure (13, 14) (*SI Appendix*, section S3). In contrast, from quench SMS, we can relate IS and QS to the oxidation states of Fe, because near 0 GPa, both Fe^{2+} and Fe^{3+} should be high spin in bridgmanite, and the effects from Fe in different crystallographic sites on the Mössbauer parameters are much less significant than the oxidation states (15) (*SI Appendix*, section S3). The IS and QS of bridgmanite are also well known at 1 bar with good agreement among existing studies (2, 4, 5) (*SI Appendix*, section S3 and Fig. S4). Because bridgmanite is metastable at ambient conditions, iron in the phase could be easily oxidized by air or moisture. Therefore, quench SMS were performed for the samples in an inert medium (Ar or Ne) in the DAC at 0–3 GPa.

We found that the quench SMS spectra of bridgmanite synthesized at 47–63 GPa are distinct from the spectra at lower and higher pressures (Fig. 1*A* and *SI Appendix*, Fig. S3). The spectra in this pressure range have much more well-defined quantum beats compared with those in other pressure ranges. The synthetic SMS spectrum of Fe^{2+}-rich bridgmanite agrees well with the measured SMS spectra of bridgmanite synthesized at the pressure range (Fig. 1*A*). Our spectral fitting showed that $Fe^{3+}/\sum Fe$ drops to 13–22% at 47–63 GPa, whereas it is ~60% at lower and higher pressures (Fig. 2 and *SI Appendix*, Fig. S4 and Table S1). Our glass-starting material contains 10% of $Fe^{3+}/\sum Fe$, similar to the $Fe^{3+}/\sum Fe$ observed at 51–63 GPa. This similarity means that the system does not produce Fe^{3+} over this pressure range. The other Mössbauer parameters, QS and IS, are in agreement with the previous studies (*SI Appendix*, Fig. S4*B*), indicating that the changes found in the spectra originated from Fe^{3+} content.

Among the recovered samples for SMS, one synthesized at 47 GPa (Figs. 1 and 2) was sufficiently thinned for electron energy loss spectroscopy (EELS) (Fig. 3). EELS can measure $Fe^{3+}/\sum Fe$ through energy changes during electronic transitions, which is a completely different physical process compared with SMS. Therefore, EELS provides an independent determination of $Fe^{3+}/\sum Fe$ in bridgmanite, complementing the SMS data analysis which can be sensitive to starting models. However, the intense electron beam is known to alter $Fe^{3+}/\sum Fe$ during EELS measurements, even for minerals stable at ambient conditions (16). Therefore, we optimized EELS parameters until we found no changes in $Fe^{3+}/\sum Fe$ of the standard mineral specimens: olivine, andradite, and cronstedtite (Fig. 3). All of the EELS spectra measured for the sample showed negligible spectral signatures from Fe^{3+} in both L_2 and L_3, indicating that iron in the sample is predominantly Fe^{2+} (Fig. 3). Spectral fitting indicated that $Fe^{3+}/\sum Fe$ should be $<10\%$, which agrees with our quench SMS for the same sample.

Our $Fe^{3+}/\sum Fe$ at the lowest pressure (35 GPa) agrees well with the multianvil results (1, 5) on aluminous bridgmanite under reducing conditions at 26 GPa (Fig. 2). There are three other datasets from laser-heated DAC (LHDAC) experiments (7–9), which have a wide enough pressure range for comparison with our dataset, although these datasets have fewer data points, with larger gaps between the points (Fig. 2). None of these three datasets show a clear drop in $Fe^{3+}/\sum Fe$ at 47–63 GPa. However, there are a few important differences in the experiments. The chemical compositions of these three datasets are all different from each other and also from our study (see *SI Appendix* for details). The three data points in Sinmyo et al. (7) all have different chemical compositions. A data point at 93 GPa in Piet et al. (9) was obtained from a different starting material with much more Al. Prescher et al. (8) used Fe^{3+}-rich bridgmanite synthesized at 25 GPa as a starting material, which is different from our study and the other two (7, 9), where starting materials were amorphous. Unlike amorphous starting materials, which are highly metastable at high pressure and therefore affected less by kinetic effects during high-temperature synthesis of bridgmanite, conversion from Fe^{3+}-rich to Fe^{2+}-rich bridgmanite would

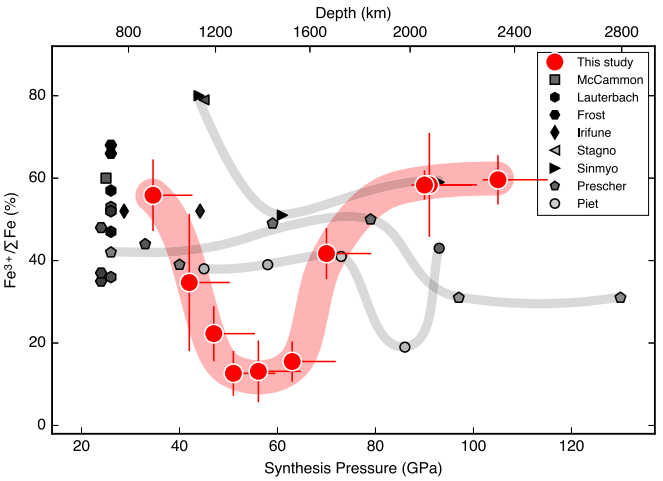

Fig. 2. Ferric iron content of aluminous bridgmanite. The parameters were measured for the samples quenched to 0–3 GPa. The gray scale for the symbols of the previous data points (1, 2, 4–8) represents Al# for 3O basis bridgmanite formula (black for Al# $\geq$ 0.1). We plot only Al# $\geq$ 0.05, except for Piet et al. (9). The light red and gray curves are guides for the eye for the datasets from this study and other studies (7–9), respectively.

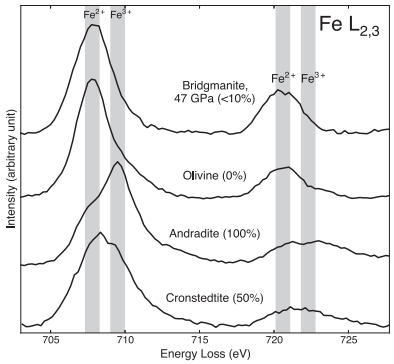

Fig. 3. EELS of Fe in bridgmanite. The sample was recovered from 47 GPa and 2,000 K and compared with olivine ($Fe^{3+}/\sum Fe = 0\%$), andradite ($Fe^{3+}/\sum Fe = 100\%$), and cronstedtite ($Fe^{3+}/\sum Fe = 50\%$). All of the spectra were measured under the same instrumental conditions (*Materials and Methods*). The structure at 708 keV in andradite is a prepeak of Fe^{3+}.

have a higher kinetic barrier to overcome. We loaded metallic Fe to ensure the reducing conditions during synthesis. None of the three studies loaded metallic Fe. However, Sinmyo et al. (7) observed metallic iron after synthesis. Therefore, the redox conditions for the dataset from the study might be comparable to our dataset. Despite these differences and fewer data points, it is interesting that all three datasets suggest a possible decrease in $Fe^{3+}/\sum Fe$ (by 20–30%) in the midmantle (Fig. 2). The different experimental methods and composition may contribute to the different pressures in the $Fe^{3+}/\sum Fe$ decrease and its magnitude observed in the datasets (7–9).

The drop of $Fe^{3+}/\sum Fe$ found here (Fig. 2) requires changes in substitution mechanisms in bridgmanite with pressure (Fig. 4*B*). Existing data (1, 5) suggest that the dominant factors for high $Fe^{3+}/\sum Fe$ in bridgmanite at 25–30 GPa are the $^{VIII}Fe^{3+}$–$^{VI}Al^{3+}$ charge-coupled substitution [where VIII and VI represents the eight (or A) and six (or B) coordinated sites in a perovskite-type structure, respectively] and charge disproportionation (*SI Appendix*, Reaction S2). Previous studies also indicate smaller but important contributions from the $^{VIII}Al^{3+}$–$^{VI}Al^{3+}$ charge-coupled substitution (*SI Appendix*, Reaction S5) and oxygen vacancy substitution (*SI Appendix*, Reaction S6) at 25–26 GPa, even when bridgmanite contains equal amounts of Al and Fe (*SI Appendix*, section S4). With an increase in pressure between 25 and 51 GPa, oxygen vacancies are expected to disappear (11) (*SI Appendix*, Reaction S10), and the $^{VIII}[Al^{3+}]$–$^{VI}[Al^{3+}]$ configuration (*SI Appendix*, Reaction S11) may become energetically more favorable than the $^{VIII}[Fe^{3+}]$–$^{VI}[Al^{3+}]$ configuration, leading to minimum $Fe^{3+}/\sum Fe$ at 53–63 GPa. The proposed change may be driven by smaller volume of the $^{VIII}[Al^{3+}]$–$^{VI}[Al^{3+}]$ configuration. Such a configuration will increase the content of Al in the A site, which decreases the volume of the A site where larger-sized Mg and Fe existed. It will also decrease the content of Al in the B site, which reduces the volume of the B site by increasing in the content of smaller-sized Si. However, conversion of Fe^{3+} to Fe^{2+} would increase the volume of the A site. Our in situ SMS indicates the appearance of a new Fe site with *QS* as high as 4 mm/s at the pressure where $Fe^{3+}/\sum Fe$ rapidly decreases (42 GPa; Fig. 1*B* and *SI Appendix*, Fig. S5), suggesting either changes in spin state or local structure for Fe^{2+} in the A site (*SI Appendix*, section S4.5). If such changes can decrease the ionic radius of Fe^{2+}, it will further stabilize the $^{VIII}[Al^{3+}]$–$^{VI}[Al^{3+}]$ configuration and therefore decrease $Fe^{3+}/\sum Fe$. At 25–50 GPa, Fe^{3+} would remain in the A site (*SI Appendix*, section S4.5).

Ferric iron in the B site undergoes a high- to low-spin transition at 50–70 GPa (10, 14). If this spin transition results in a smaller ionic radius of Fe^{3+}, likely comparable with that of Al^{3+}, the charge disproportionation would become more stable, and $Fe^{3+}/\sum Fe$ would increase by stabilization of the $^{VIII}[^{HS}Fe^{3+}, Al^{3+}]$–$^{VI}[^{LS}Fe^{3+}, Al^{3+}]$ configuration (Fig. 4*A* and *SI Appendix*, section S4.7). We calculated the volume change in charge disproportionation of Fe to such a configuration (*SI Appendix*, Fig. S8*C* and section S4.7) and found that the volume of the $^{VIII}[^{HS}Fe^{3+}, Al^{3+}]$–$^{VI}[^{LS}Fe^{3+}, Al^{3+}]$ configuration is significantly smaller, supporting the proposed change in the substitution mechanism at pressures >70 GPa.

Our results indicate that almost all of the iron in bridgmanite is ferrous (Fe^{2+}), with little ferric (Fe^{3+}) iron at 1,100- to 1,700-km depths (hereafter low ferric iron bridgmanite zone; LIBZ), whereas bridgmanite in the lower mantle regions above and below LIBZ contains >50% of iron in the ferric oxidation state (hereafter high ferric iron bridgmanite zone; HIBZ). Because Fe^{2+} partitions into ferropericlase, whereas almost all Fe^{3+} enters bridgmanite (2), bridgmanite will be depleted in Fe in LIBZ (also can be referred to as low-iron bridgmanite zone) compared with HIBZs (also can be referred to as high-iron bridgmanite zone), and ferropericlase will have an increased amount of Fe in LIBZ compared with HIBZs (Fig. 4*B*).

A number of studies have been conducted to compare the density and velocity profiles of compositional models (pyrolite) with seismic observations. However, these models have assumed that the compositions of individual minerals, in particular Fe content and oxidation state, do not change throughout the lower mantle (18–20). Both experiments and computations have found that the bulk modulus (and therefore bulk sound speed) of ferropericlase decreases considerably within the pressure range where the phase is in a transitional state from high spin to low spin (therefore, a mixed-spin state), although the bulk modulus of ferropericlase with high-spin Fe is essentially the same as that with low spin (18–21). In contrast, the spin transition has no significant impact on density and shear velocity profiles (18–21).

The bulk sound speed profile of pyrolite along the mantle geotherm shows significant discrepancy with seismic values if it is calculated by assuming constant $Fe^{3+}/\sum Fe$ in bridgmanite (therefore constant mineral compositions) throughout the lower mantle. As shown in Fig. 4*A*, such discrepancies are clear at 1,300- to 1,800-km and 2,100- to 2,400-km depths, if bridgmanite is rich in Fe^{3+} and Fe^{2+} (and therefore ferropericlase has low and high Fe contents), respectively, throughout the lower mantle (see *Materials and Methods* for details). Although the bulk sound speed depression should be detectable, such large-scale structures have not been found in the lower mantle (22). Decreasing the content of ferropericlase provides a substantially better fit. However, the required decrease increases the bulk sound speed of mineralogical models above the seismic values throughout the lower mantle and results in a much lower Mg/Si ratio for the lower mantle than the upper mantle. The change in Mg/Si ratio would make the lower mantle nonpyrolitic as a result, making the lower mantle richer in Si.

We include the observed $Fe^{3+}/\sum Fe$ change in the calculation (the red curve in Fig. 4*A*). From the iron partition coefficients for Fe^{2+}- and Fe^{3+}-rich bridgmanite (2, 23), we obtained 0.27 and 0.15 Fe# of ferropericlase (for 1 oxygen base chemical formula) in LIBZ and HIBZs for pyrolite composition in response to the Fe oxidation state change in bridgmanite, respectively (see *Materials and Methods* for details). The higher Fe content in ferropericlase in LIBZ (0.27 Fe#) will significantly increase the spin transition pressure for the Fe (18, 20). As shown in Fig. 4*A* (blue curves), because the spin transition does not occur until much greater depths, ferropericlase with higher Fe content in LIBZ will have only high-spin Fe^{2+}. Ferropericlase (with lower Fe content) in HIBZs would not decrease bulk sound speed significantly, because the mixed-spin state, which causes the severe bulk modulus decrease for 0.15 Fe#, occurs at the depths of LIBZ. Instead, ferropericlase has almost all Fe^{2+} in high spin in shallow

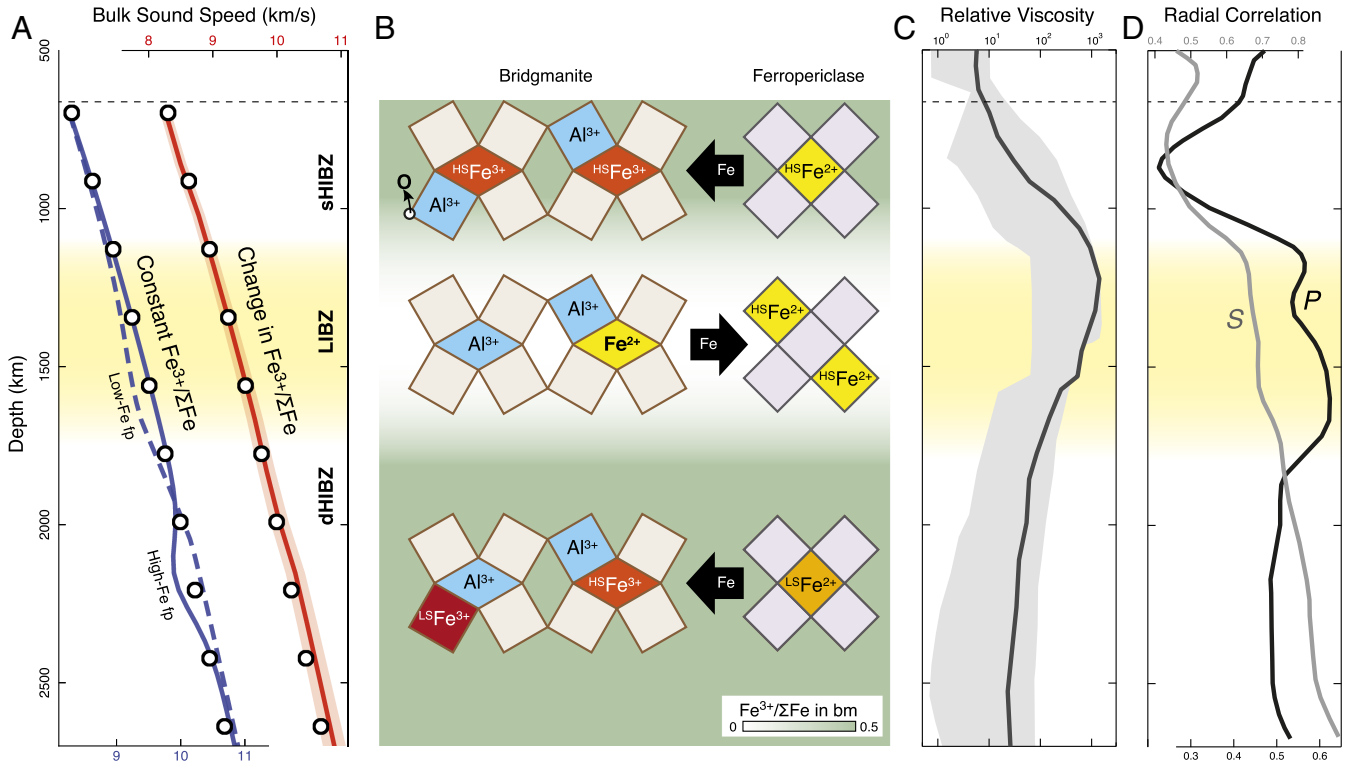

Fig. 4. Seismic and mineralogical structures in the lower mantle. (*A*) Comparison of bulk sound speeds of seismic measurement [PREM (17); circles] and pyrolite models. Three different pyrolitic models are presented: depth-dependent changes in $Fe^{3+}/\sum Fe$ of bridgmanite (red curve), constant Fe in bridgmanite (0.04Fe^{2+}#) and ferropericlase (0.27Fe#) (solid blue curve), and constant Fe in bridgmanite (0.045Fe^{2+}# and 0.045Fe^{3+}#) and ferropericlase (0.15Fe#) (dashed blue curve). See *Materials and Methods* for details. The light red area represents estimated uncertainties, including those from thermoelastic parameters. (*B*) Changes in the crystal chemistry of bridgmanite and ferropericlase. For bridgmanite, the tilted squares and the diamond-shaped areas between them represent the B and A sites, respectively. For ferropericlase, the 45° rotated squares represent the MgO_6 octahedra. (*C*) Changes in viscosity (26). The black curve is for a density scaling of 0.2 and harmonic degrees of 2–7. The light gray area represents a range of different values found in all of the models in ref. 26. (*D*) Changes in radial correlations of the *P* and *S* wave tomography models (PMEAN and SMEAN) (27).

HIBZ at 660- to 1,100-km depths and low spin in the deep HIBZ at 1,700- to 2,900-km depths.

Unlike the models without the bridgmanite $Fe^{3+}/\sum Fe$ change, we found no significant reduction in the bulk sound speed profile of pyrolite when we incorporate the observed $Fe^{3+}/\sum Fe$ change in the calculation (Fig. 4*A*). The bulk sound profile of pyrolite with the bridgmanite $Fe^{3+}/\sum Fe$ change agrees well with average [preliminary reference Earth model (PREM)] seismic values for the lower mantle (17). We also found that the density profile of pyrolite agrees well with seismic values (*SI Appendix*, Fig. S10). $Fe^{3+}/\sum Fe$ in bridgmanite decreases and increases above and below LIBZ over a pressure interval of 10–20 GPa. Such a gradual change will not result in any sharp changes in the lower mantle seismic profiles, consistent with the absence of global seismic discontinuities in the 1,000- to 2,000-km depth interval.

We showed that the reduction of Fe^{3+} in bridgmanite at 1,100- to 1,700-km depths reconciles the discrepancy in bulk sound speed profile between pyrolitic lower-mantle composition and seismic observations. Therefore, there is no need for differences in major element chemistry between the upper and lower mantle, consistent with seismic observations of slabs penetrating to the lowermost mantle and therefore whole mantle convection (24).

An important unknown in the model above is possible compositional sensitivity of the depth interval for the $Fe^{3+}/\sum Fe$ drop in bridgmanite. A recent Brillouin spectroscopy study (25) found good agreement in velocities between Fe^{3+}-rich bridgmanite in $Mg_{0.9}Fe_{0.1}Al_{0.1}Si_{0.9}O_3$ and seismic 1D model (PREM) at pressures expected for the shallower lower mantle. However, the velocities of Fe^{3+}-rich bridgmanite showed significant mismatch with the seismic model at depths >1,300 km, while Fe^{2+}-rich bridgmanite agrees better with the seismic model in the region. The observations led to a proposal that $Fe^{3+}/\sum Fe$ in bridgmanite decreases at the depth range. The proposed depth is remarkably similar to the depth expected for the $Fe^{3+}/\sum Fe$ drop in bridgmanite found in our study (1,100 km), despite the difference in the total Fe content.

Recently, elevated viscosity has been reported (26) near the depth of low-Fe^{3+} bridgmanite (LIBZ) (Fig. 4*C*). Most *P*-wave tomographic models (27) have also shown a transition from minimum radial correlation of seismic structures at 700–1,000 km to enhanced correlation at depths greater than ∼1,500 km (Fig. 4*D*). Recent tomographic models have found stagnation or broadening of some subducting slabs (28) and horizontal deflections of some mantle plumes (29) near this depth range. Numerical simulations demonstrated that the viscosity elevation at 1,000–1,500 km can produce such seismic observations (26).

Being the dominant phase in the region (70 vol%), bridgmanite controls the viscosity of the lower mantle (30). According to our study, bridgmanite in LIBZ at 1,100–1,700 km contains little or no Fe^{3+} and therefore a lower amount of Fe because of strong partitioning of Fe^{2+} to ferropericlase. Although the effect of Fe is still unknown for the viscosity of bridgmanite due to technical difficulties, iron can decrease viscosity as shown in other minerals (31). Because iron reduces the melting temperature of bridgmanite and viscosity can be scaled to homologous temperature (temperature normalized to material's melting temperature) (32), low-Fe content bridgmanite at 1,100–1,700 km would have a high viscosity, providing a plausible explanation for

the viscosity increase (26) without invoking any major changes in chemical composition over this depth range.

Materials and Methods

Starting Materials. We used two different starting materials with the same composition: 28.8 wt% MgO, 53.6 wt% SiO_2, 12.8 wt% FeO, and 4.8 wt% Al_2O_3. We synthesized 15 bridgmanite samples (*SI Appendix*, Table S1). For the 3-oxygen formula unit of bridgmanite, the synthesized bridgmanite contained 0.19Fe and 0.10Al, which are both elevated from the samples studied previously, including pyrolitic compositions. The elevated amounts of Fe are important to obtaining sufficient quality of Mössbauer spectra for accurate determination of the oxidation state of Fe. Our Al/Fe ratio overlaps with the range of the values reported for bridgmanite synthesized from pyrolitic starting materials (2, 7, 8, 33). The $Fe^{3+}/\sum Fe$ of bridgmanite synthesized at the lowest pressure of our study (35 GPa) followed the trends found in bridgmanite reported in previous redox-controlled experiments (1, 5) (see *SI Appendix*, Fig. S7 and sections S4.1–S4.4 for detailed discussion). Both starting materials are enriched with ^{57}Fe: 67 and 95% for pyroxene and glass-starting materials, respectively. The SMS data of these materials indicate that the pyroxene contains no detectable amount of Fe^{3+} and the glass-starting material contains $Fe^{3+}/\sum Fe \simeq 10\%$ (*SI Appendix*, Fig. S3 and section S3).

Sample Preparation. To ensure reducing conditions, we mixed our starting materials with predried Fe metal powder (2–5 wt%) following the method used in multianvil syntheses by Frost et al. (1) (*SI Appendix*, Figs. S1 and S9). A potential disadvantage of mixing metallic Fe with the starting materials is the complexity of measured SMS due to Mössbauer signal from Fe in both metal and bridgmanite. To reduce the problem, we used metallic Fe with a natural level ^{57}Fe (2%) and starting materials with ^{57}Fe enrichment (67–95%). We also limited the amount of metallic iron to $\leq$5 wt%. The powder mixture was compressed between diamond anvils to make a rigid foil. The foil was loaded into the hole in a preindented Re gasket. The foil was propped by three to four grains of the starting materials to allow Ar or Ne to flow in to separate the foil from the diamond anvils during cryogenic or gas loading (*SI Appendix*, Table S1). The separation of the sample foil from the diamond anvils is particularly important to prevent direct contact between the diamond anvils and the sample foil and therefore to ensure lower thermal gradient during laser heating. One sample was loaded with a KCl medium. The KCl was dried at 1,073 K for 24 h before loading. Some ruby chips were loaded on the gasket or the edge of the sample chamber as pressure sensors, to avoid direct contact between the ruby chips and our sample foils. Pressures were measured by using both ruby (34) and diamond pressure scales (35) after temperature quench.

High-Pressure Synthesis. At a target pressure, double-sided laser heating was conducted to 2,000–2,300 K at sectors 13 and 16, Advanced Photon Source (APS). By scanning the infrared laser beams (1,065 nm), we transformed the entire foil of the starting material + Fe metal powder mixture into bridgmanite + Fe metal powder. The size of hot spot was 20–25 μm, and the sample was translated by 2–5 μm during scanning. In the first scan, each spot was heated for 5–10 min until the starting material transformed to bridgmanite. From the second scan, each spot was heated for 1–5 min. The scan was repeated for multiples of time. Each spot was heated for a total of ∼10–30 min. Thermal radiation spectra from both sides of the sample were measured by using an imaging spectrometer and fitted to the Planck black-body radiation function to obtain temperatures. To avoid memory effects from preexisting electronic configuration of Fe and the crystal structure, once bridgmanite was formed at a target pressure, the samples were never heated again at different pressures. The pressure before and after heating was measured. We found pressure changes <5 GPa. However, pressure in the DAC during laser heating should be higher due to thermal pressure (36, 37). Previous studies have shown a ∼5 GPa increase for heating to 2,000–2,300 K (38), which is included in the estimated error bars presented in Fig. 2.

Synchrotron XRD. Diffraction patterns were measured during laser heating and after temperature quench for nine different samples at different pressures, ranging between 31 and 105 GPa, to ensure the synthesis of bridgmanite (*SI Appendix*, Fig. S2). The measurements were conducted at beamlines 13IDD (39) and 16IDB (40) of the APS. At GSECARS, monochromatic X-ray beams with a wavelength of 0.3344 Å were focused to an area of $3 \times 4\ \mu m^2$ on the sample in LHDAC. At the High-Pressure Collaborative Access Team (HPCAT), monochromatic X-ray beams with a wavelength of 0.3515 Å were focused to an area of $5 \times 6\ \mu m^2$ on the sample in LHDAC. Powder diffraction images were collected by using MarCCD detectors. The laser beams were aligned coaxially with the X-ray beam.

SMS. Nuclear forward scattering was conducted at sector 3 of APS (Fig. 1 and *SI Appendix*, Fig S3). A 14.4-keV X-ray beam was focused on an area of $6 \times 6\ \mu m^2$ in the sample. The storage ring was operated in top-up mode with 24 bunches separated by 153 ns. Nuclear resonant scattering was measured in a time window of 15–130 ns with a typical data collection time of 8–12 h. We conducted SMS on both the temperature-quenched samples at high pressure (in situ SMS) and decompressed samples at 0–3 GPa in DAC (quench SMS). A total of 14 samples were successfully measured at in situ high pressure in DAC after laser heating. Ten samples were successfully quenched to 0–3 GPa, where SMS was conducted. The spectral fitting was performed by using the CONUSS package (41) (see *SI Appendix*, section S3 for details).

EELS. We expanded the beam size at the sample to 100–200 nm in a transmission electron microscope (TEM) mode with sufficiently low accelerating voltage at 120 kV to reduce the electron dosage of the sample, while allowing enough total intensity to provide good signal-to-noise ratios for the spectra. The measurements were performed in a JEOL ARM200 ACEM with a Gatan Enfinium spectrometer. The energy resolution was 0.7–0.9 eV. We avoided the area with metallic iron grains to obtain the EELS spectra from pure bridgmanite. We also measured the EELS spectra of minerals with known oxidation states of Fe (olivine, pyroxene, andradite, and cronstedtite) using the same instrumental conditions and used them for spectral fitting to extract $Fe^{3+}/\sum Fe$. The fraction of ferric iron ($Fe^{3+}/\sum Fe$) was determined by the EELS analysis methods in ref. 42.

EDS. The measurements were conducted in a JEOL ARM200 ACEM for spot measurements and a JEOL JEM-2800 TEM for X-ray mapping (*SI Appendix*, Fig. S9). In ARM, EDS was performed with a JEOL 50 mm^2 windowless light-element-sensitive X-ray detector. The X-ray compositional mapping was conducted in a JEOL JEM-2800 system combined with a JED-2300T detector at 200 kV. The beam size was 0.5 nm. The EDS spectra were analyzed by using the method in ref. 43.

Lower-Mantle 1D Profile Calculations. The bulk sound speed and density profiles were calculated for pyrolite by using the Burnman toolkit (44) combined with the parameters listed in *SI Appendix*, Table S2 (14, 45, 45–47) along the mantle geotherm (48). We corrected volume and elasticity for compositional differences using a linear assumption. We assumed that thermal parameters were not sensitive to compositional differences.

We conducted calculations for a CaO–MgO–Al_2O_3–SiO_2–FeO system with oxide ratios from the pyrolite composition in Ringwood (49). The bulk composition was fixed throughout the lower mantle for all of the pyrolite profiles we calculated. Iron partition coefficients were 0.58 (2) and 0.12 (23) for Fe^{3+}-rich (HIBZs) and Fe^{2+}-rich (LIBZ) bridgmanite systems, respectively. From the partition coefficients and the pyrolite composition, we obtained: $0.045Fe^{3+}$# and $0.045Fe^{2+}$# in bridgmanite and 0.15Fe# in ferropericlase for HIBZs, and $0.04Fe^{2+}$# in bridgmanite and 0.27Fe# in ferropericlase for LIBZ. All Al_2O_3 entered bridgmanite, and all CaO was incorporated into $CaSiO_3$ perovskite in our models.

Our Fe# values for bridgmanite and ferropericlase in HIBZ were consistent with the Fe# reported for pyrolite with Fe^{3+}-rich bridgmanite in Irifune et al. (2), 0.09–0.10 and 0.12–0.14, respectively. Ferropericlase in the study had slightly lower Fe# than ours because it contained other cations, such as Si, Al, Ni, Cr, and Na, the total content of which was 0.02–0.06 cation#. In our calculation, we assumed that Si and Al did not enter ferropericlase and did not consider minor oxide components with weight percent less than 1%.

The bulk sound speed and density of ferropericlase were calculated for their corresponding iron contents (0.15 and 0.27 Fe# in Fig. 4*A* and *SI Appendix*, Fig. S10). We calculated the softening of bulk modulus (reduction of bulk sound speed) in ferropericlase in mixed spin using the methods and parameters presented in previous studies (18, 20). Both theory and experiments have shown that spin transition pressure increases with Fe content in ferropericlase (50–53). Temperature also increases the spin transition pressure and the interval of the spin transition zone (54, 55). Therefore, we consider data obtained at high pressure–temperature (18, 20). Because there are no direct measurements for our two compositions, we adapted the spin transition pressures reported for 0.1875 and 0.25 Fe# ferropericlase at mantle-related high temperatures (18, 20) for 0.15 (HIBZ) and 0.27 (LIBZ) Fe#, respectively. Density profiles of all three presented pyrolite models are in agreement, consistent with previous results (18, 20), in that ferropericlase

spin transition does not have significant impact on density (*SI Appendix*, Fig. S10).

ACKNOWLEDGMENTS. Discussions with E. Garnero, A. McNamara, J. Tyburczy, K. Leinenweber, and T. Duffy improved the manuscript. J. Mardinly and A. Toshi assisted with the ACEM measurements. H. Hashiguich at JEOL Ltd. assisted with sample preparation for TEM and ACEM analysis. This work was supported by NSF Grants EAR1316022 and EAR1338810 (to S.-H.S.). Synchrotron measurements were conducted at the Advanced Photon Source, a Department of Energy (DOE) Office of Science User Facility operated for the DOE Office of Science by Argonne National Laboratory under Contract DE-AC02-06CH11357. XRD measurements were performed at GeoSoilEnviroCARS and HPCAT, APS, ANL. GeoSoilEnviroCARS is supported by NSF Grant EAR-1128799 and DOE Grant DE-FG02-94ER14466. HPCAT is supported by DOE-NNSA Grant DE-NA0001974 and DOE-BES Grant DE-FG02-99ER45775.

1. Frost DJ, et al. (2004) Experimental evidence for the existence of iron-rich metal in the Earth's lower mantle. *Nature* 428:409–412.
2. Irifune T, et al. (2010) Iron partitioning and density changes of pyrolite in Earth's lower mantle. *Science* 327:193–195.
3. Navrotsky A, et al. (2003) Aluminum in magnesium silicate perovskite: Formation, structure, and energetics of magnesium-rich defect solid solutions. *J Geophys Res* 108:2330.
4. McCammon C (1997) Perovskite as a possible sink for ferric iron in the lower mantle. *Nature* 387:694–696.
5. Lauterbach S, McCammon CA, van Aken P, Langenhorst F, Seifert F (2000) Mössbauer and ELNES spectroscopy of (Mg,Fe)(Si,Al)O_3 perovskite: A highly oxidised component of the lower mantle. *Contrib Mineral Petr* 138:17–26.
6. Stagno V, et al. (2011) The stability of magnesite in the transition zone and the lower mantle as function of oxygen fugacity. *Geophys Res Lett* 38:L19309.
7. Sinmyo R, Hirose K, Muto S, Ohishi Y, Yasuhara A (2011) The valence state and partitioning of iron in the Earth's lowermost mantle. *J Geophys Res* 116:B07205.
8. Prescher C, Langenhorst F, Dubrovinsky LS, Prakapenka VB, Miyajima N (2014) The effect of Fe spin crossovers on its partitioning behavior and oxidation state in a pyrolitic Earth's lower mantle system. *Earth Planet Sci Lett* 399:86–91.
9. Piet H, et al. (2016) Spin and valence dependence of iron partitioning in Earth's deep mantle. *Proc Natl Acad Sci USA* 113(40):11127–11130.
10. Xu S, Shim SH, Morgan D (2015) Origin of Fe^{3+} in Fe-containing, Al-free mantle silicate perovskite. *Earth Planet Sci Lett* 409:319–328.
11. Brodholt JP (2000) Pressure-induced changes in the compression mechanism of aluminous perovskite in the Earth's mantle. *Nature* 407:620–622.
12. Badro J, et al. (2004) Electronic transitions in perovskite: Possible nonconvecting layers in the lower mantle. *Science* 305:383–386.
13. McCammon C, et al. (2008) Stable intermediate-spin ferrous iron in lower-mantle perovskite. *Nat Geosci* 1:684–687.
14. Catalli K, et al. (2011) Effects of the Fe^{3+} spin transition on the properties of aluminous perovskite – new insights for lower-mantle seismic heterogeneities. *Earth Planet Sci Lett* 310:293–302.
15. Dyar MD, Agresti DG, Schaefer MW, Grant CA, Sklute EC (2006) Mössbauer spectroscopy of earth and planetary materials. *Annu Rev Earth Planet Sci* 34:83–125.
16. Garvie LAJ, Zega TJ, Rez P, Buseck PR (2004) Nanometer-scale measurements of $Fe^{3+}/\sum$Fe by electron energy-loss spectroscopy: A cautionary note. *Am Mineral* 89:1610–1616.
17. Dziewonski AM, Anderson DL (1981) Preliminary reference Earth model. *Phys Earth Planet Inter* 25:297–356.
18. Wentzcovitch RM, et al. (2009) Anomalous compressibility of ferropericlase throughout the iron spin cross-over. *Proc Natl Acad Sci USA* 106:8447–8452.
19. Marquardt H, Speziale S, Reichmann HJ, Frost DJ, Schilling FR (2009) Single-crystal elasticity of ($Mg_{0.9}Fe_{0.1}$)O to 81 GPa. *Earth Planet Sci Lett* 287:345–352.
20. Mao Z, Lin JF, Liu J, Prakapenka VB (2011) Thermal equation of state of lower-mantle ferropericlase across the spin crossover. *Geophys Res Lett* 38:L23308.
21. Crowhurst JC, Brown JM, Goncharov AF, Jacobsen SD (2008) Elasticity of (Mg,Fe)O through the spin transition of iron in the lower mantle. *Science* 319:451–453.
22. Cammarano F, Marquardt H, Speziale S, Tackley TJ (2010) Role of iron-spin transition in ferropericlase on seismic interpretation: A broad thermochemical transition in the mid mantle? *Geophys Res Lett* 37:L03308.
23. Nakajima Y, Frost DJ, Rubie DC (2012) Ferrous iron partitioning between magnesium silicate perovskite and ferropericlase and the composition of perovskite in the Earth's lower mantle. *J Geophys Res* 117:B08201.
24. van der Hilst RD, Widiyantoro S, Engdahl ER (1997) Evidence for deep mantle circulation from global tomography. *Nature* 386:578–584.
25. Kurnosov A, Marquardt H, Frost DJ, Ballaran TB, Ziberna L (2017) Evidence for a Fe^{3+}-rich pyrolitic lower mantle from (Al,Fe)-bearing bridgmanite elasticity data. *Nature* 543:543–546.
26. Rudolph ML, Lekić V, Lithgow-Bertelloni C (2015) Viscosity jump in Earths mid-mantle. *Science* 350:1349–1352.
27. Becker TW, Boschi L (2002) A comparison of tomographic and geodynamic mantle models. *Geochem Geophys Geosys* 3(1): 2001GC000168.
28. Fukao Y, Obayashi M (2013) Subducted slabs stagnant above, penetrating through, and trapped below the 660 km discontinuity. *J Geophys Res* 118:5920–5938.
29. French SW, Romanowicz B (2015) Broad plumes rooted at the base of the Earth's mantle beneath major hotspots. *Nature* 525:95–99.
30. Girard J, Amulele G, Farla R, Mohiuddin A, Karato S-i (2016) Shear deformation of bridgmanite and magnesiowüstite aggregates at lower mantle conditions. *Science* 351:144–147.
31. Zhao YH, Zimmerman ME, Kohlstedt DL (2009) Effect of iron content on the creep behavior of olivine: 1. Anhydrous conditions. *Earth Planet Sci Lett* 287:229–240.
32. Weertman J, Weertman JR (1975) High temperature creep of rock and mantle viscosity. *Annu Rev Earth Planet Sci* 3:293–315.
33. Murakami M, Hirose K, Sata N, Ohishi Y (2005) Post-perovskite phase transition and mineral chemistry in the pyrolitic lowermost mantle. *Geophys Res Lett* 32:L03304.
34. Mao HK, Xu J, Bell PM (1986) Calibration of the ruby pressure gauge to 800 kbar under quasihydrostatic conditions. *J Geophys Res* 91:4673–4676.
35. Akahama Y, Kawamura H (2004) High-pressure Raman spectroscopy of diamond anvils to 250 GPa: Method for pressure determination in the multimegabar pressure range. *J Appl Phys* 96:3748–3751.
36. Heinz DL (1990) Thermal pressure in the laser-heated diamond anvil cell. *Geophys Res Lett* 17:1161–1164.
37. Andrault D, et al. (1998) Thermal pressure in the laser-heated diamond-anvil cell: An X-ray diffraction study. *Eur J Mineral* 10:931–940.
38. Shim SH, Duffy TS, Shen G (2000) The stability and P–V–T equation of state for $CaSiO_3$ perovskite in the Earth's lower mantle. *J Geophys Res* 105:25955–25968.
39. Prakapenka VB, et al. (2008) Advanced flat top laser heating system for high pressure research at GSECARS: Application to the melting behavior of germanium. *High Press Res* 28:225–235.
40. Meng Y, Shen G, Mao HK (2006) Double-sided laser heating system at HPCAT for insitu x-ray differentiation at high pressures and high temperatures. *J Phys Condens Matter* 18:S1097–S1103.
41. Sturhahn W (2000) CONUSS and PHOENIX: Evaluation of nuclear resonant scattering data. *Hyperfine Interact* 125:149–172.
42. van Aken PA, Liebscher B (2002) Quantification of ferrous/ferric ratios in minerals: New evaluation schemes of Fe L 23 electron energy-loss near-edge spectra. *Phys Chem Mineral* 29:188–200.
43. Cappellen EV, Doukhan E (1994) Quantitative transmission X-ray microanalysis of ionic compounds. *Ultramicroscopy* 53:343–349.
44. Cottaar S, Heister T, Rose I, Unterborn C (2014) Burnman - a lower mantle mineral physics toolkit. *Geochem Geophys Geosys* 15(4):1164–1179.
45. Lundin S, et al. (2008) Effect of Fe on the equation of state of mantle silicate perovskite over 1 Mbar. *Phys Earth Planet Inter* 168:97–102.
46. Stixrude L, Lithgow-Bertelloni C (2011) Thermodynamics of mantle minerals - II. Phase equilibria. *Geophys J Int* 184:1180–1213.
47. Murakami M, Ohishi Y, Hirao N, Hirose K (2012) A perovskitic lower mantle interred from high-pressure, high-temperature sound velocity data. *Nature* 485:90–94.
48. Brown JM, Shankland TJ (1981) Thermodynamic parameters in the Earth as determined from seismic profiles. *Geophys J R Astron Soc* 66:576–596.
49. Ringwood AE (1975) *Composition and Petrology of the Earth's Mantle* (McGraw-Hill, New York), p 618.
50. Persson K, Bengtson A, Ceder G, Morgan D (2006) Ab initio study of the composition dependence of the pressure-induced spin transition in the ($Mg_{1-x}Fe_x$)O system. *Geophys Res Lett* 33:L16306.
51. Fei Y, et al. (2007) Spin transition and equation of state of (Mg,Fe)O solid solution. *Geophys Res Lett* 34:L17307.
52. Badro J (2014) Spin transitions in mantle minerals. *Annu Rev Earth Planet Sci* 42: 231–248.
53. Lin JF, Speziale S, Mao Z, Marquardt H (2013) Effects of the electronic spin transitions of iron in lower mantle minerals: Implications for deep mantle geophysics and geochemistry. *Rev Geophys* 51:244–275.
54. Sturhahn W, Jackson JM, Lin JF (2005) The spin state of iron in minerals of Earth's lower mantle. *Geophys Res Lett* 32:L12307.
55. Lin JF, et al. (2007) Spin transition zone in Earth's lower mantle. *Science* 317: 1740–1743.